Article

Study on Performance and Operation Mechanism of a Separation Equipment for a PWR Steam Generator

Xuelong Yang *, Chenbing Zhu, Qiwei Zhou, Jianchong Chen and Jiegang Mou *

College of Metrology and Measurement Engineering, China Jiliang University, Hangzhou 310018, China
*   Correspondence: yxl@cjlu.edu.cn (X.Y.); mjg@cjlu.edu.cn (J.M.)

Abstract: Computational fluid dynamics (CFD) is adopted to calculate and analyze the performance and separation mechanism of a steam-water separation equipment for a pressurized water reactor (PWR) steam generator. The steam-water two-phase flow is simulated by the Euler two-fluid model, and several representative water droplet diameters are selected among 50 to 400 μm. The influence mechanism of water droplet diameter on the performance is investigated by analyzing the flow parameters such as phase volume fraction, velocity, and turbulent kinetic energy. The results show that the integrated calculation and analysis of the separation equipment can more truly reflect the flow state between the separators, improving the reliability of the performance prediction and mechanism analysis. With the increase in water droplet diameter, the separation efficiency of the separation equipment and each separator gradually increases, the outlet wetness gradually decreases, and the pressure loss first decreases and then stabilizes. When 400 μm is taken as the characteristic value of the actual droplet diameter distribution at the inlet of the separation equipment, the performance prediction is more accurate, the pressure loss of each separator is relatively close, and the pressure loss of the primary separator is less affected by the droplet diameter and smaller than that of the swirl-vane primary separator, which is conducive to achieving a higher circulation ratio (*CR*). Re-entrainment occurs at the perforations of the primary separator and the outlet of the secondary separator, and the corresponding structure is suggested to be optimized to further improve separation efficiency of the separation equipment.

Keywords: separator; moisture separation; steam generator; droplet; PWR; CFD

1. Introduction

Pressurized water reactor (PWR) nuclear power plants use steam generated by steam generators (SGs) to drive a turbine to generate electricity [1]. SGs are heat exchangers used to convert feed water into steam with heat produced in a nuclear reactor. Although there are many types of steam generators used in nuclear power plants, three types are widely used in PWR nuclear power plants. They are vertical U-tube natural circulation SG, horizontal natural circulation SG, and vertical once-through SG, among which the vertical U-tube natural circulation SG is the most widely used. The steam generated by the vertical once-through SG is superheated, while the steam generated by the other two SGs is saturated and contains some water. Steam with high wetness will increase the pressure loss and cause corrosion and impact on the steam turbine, affecting the economy and safety of the power plant [2]. The separation equipment is used to separate water from the wet steam to ensure that the wetness is lower than the required value [3]. It is usually composed of two-stage separators, namely, the primary separator and the secondary separator. The primary separator determines the steam wetness at the inlet of the secondary separator and the steam carry-under, while its pressure loss affects the circulation ratio (*CR*) and the steam pressure produced. The secondary separator determines the final steam quality and is the last defense of the SG. Therefore, the separation equipment is one of the key components and core technologies of the SG [3,4].

At present, the research of separation equipment is mainly based on cold and hot tests [1–3,5–8], but due to the high cost of tests, especially the hot tests, more and more scholars use the computational fluid dynamics (CFD) technology to carry out the calculation and analysis of multiphase flow and performance prediction of the separation equipment [9–14]. Zhao et al. [12] calculated and analyzed the water droplet movement pattern and separation efficiency of the primary and secondary separators in the AP1000 SG. Zhang et al. [13] used the Lagrangian-Euler simulation method to discuss droplet generation, motion, collision, wall impact, and fragmentation, and obtained a more detailed simulation method of droplet trajectory. Du et al. [14] calculated the formation of the water film in the non-hook corrugated plate, and found that the height and area of the water film reached the maximum when the humidity reached 10%, and the separation efficiency was the best. Zhu et al. [15] comprehensively considered the separation efficiency and pressure loss to optimize the drain hook structure of the double channel corrugated-plate separator. Cai [16], Li [17] and Wang [18] carried out characteristic analysis on the structure of the corrugated-plate separators through CFD, optimized structure parameters such as the number of stages and wavelength, and designed the separator with greater separation efficiency with lower pressure loss.

The separation equipment is mainly composed of a swirl-vane separator and a corrugated-plate separator, or a curved-arm separator and an axial flow separator. The former combination has a complex structure and high pressure loss, and the corresponding *CR* value of the SG with full power is between 3.1 and 4.2 [19]. The corresponding *CR* value achieved by the latter combination is above 5, up to 6, largely due to the simpler structure and lower pressure loss of the primary curved-arm separator [20–22]. The "one-to-one" combination adopted by the latter combination is applicable to the occasions of integration, compactness, and high *CR* requirements [23].

Although CFD technology has been widely used in the research of swirl-vane separators and corrugated-plate separators, it is rarely used in the research of curved-arm separators and axial flow separators, and mainly focuses on structure optimization [24,25]. The research on internal multiphase flow and separation mechanism has not been seen in the public literature. Meanwhile, the primary separator and the secondary separator were usually studied separately, without taking the outlet parameters of the primary separator as the inlet parameters of the secondary separator. The gas and droplets at the outlet of the primary separator are in a rotating state, and keep rotating when entering the secondary separator. At present, when studying the secondary separator, it is generally assumed that the gas is non-rotational and droplets are uniformly distributed in the gas. This simplification is conducive to carry out the study, but it cannot well describe the actual operation mechanism of the separation equipment. Therefore, we use CFD technology to carry out an integrated study on the separation equipment composed of a curved-arm separator and an axial flow separator under actual operating conditions to deepen our understanding of its internal multiphase flow and separation mechanism.

The multiphase flow simulation scheme of the separator is mainly based on the Euler two-fluid model [26,27] and the discrete phase model (DPM) [16–18]. The gas and droplets are assumed to be continuous and in discrete phases, respectively. The DPM model is applicable to multiphase flow with the volume fraction of discrete phases less than 10% [13], while the volume fraction of water at the inlet of the curved-arm separator is more than 13%. Therefore, the DPM model is not applicable. Water film exists in both the curved-arm separator and axial flow separator, which cannot be simulated by the DPM model. The Euler two-fluid model is not limited to the volume fraction of the discrete phase, and is adopted for the simulation of the two separators.

The forces between the two phases are calculated with the droplets inside the separator having the same diameter. Therefore, the selection of the droplet diameter plays a key and even decisive role in the accuracy of performance prediction and flow detail description of the separation equipment [26]. In actual operation, the droplets in the separation equipment exist in various diameters. The strength of the interactive forces between

the water droplets and the steam differs with droplet diameters, which affects the multiphase flow characteristics, changing the movement trajectory and destination of the water droplets. The flow pattern and energy consumption of the steam are also influenced, thus affecting the separation efficiency and pressure loss of the separation equipment. In this paper, the integrated calculation and analysis of the separation equipment under different water droplet diameters are carried out. By comparing and analyzing the distribution and variation of characteristic parameters i.e., velocity, phase distribution, and turbulent kinetic energy under different droplet diameters, the mechanism of the multiphase flow and separation and performance variation are studied. Thus, support is provided for the design and application expansion of the separation equipment and the operation of PWR.

2. Structure and Working Principle of Separation Equipment

The separation equipment (Figure 1) adopts a curved-arm separator as the primary separator, which is mainly composed of a riser tube, a curved-arm, and a return cylinder. The curved-arm is a spiral structure with clockwise rotation (viewed from top), which has four branches (arms) and is divided into three layers, forming 12 channels. The secondary separator adopts an axial flow separator, mainly including inlet vanes, a skimmer cylinder, a drain tube, and a separation box. The steam-water mixture produced by the heat transfer tubes of the SG enters the curved-arm from the riser tube and forms a rotating flow. The water droplets are thrown by the centrifugal force on the wall of the return cylinder and gather into a water film. Water film under the curved-arm flows downward along the wall of the return cylinder by the action of gravity, and the rest continues to rise along the wall by the shear stress of the steam and is discharged when it flows through the perforations. The steam leaving the primary separator carries remaining water droplets into the secondary separator. The inlet vanes of the secondary separator are arranged in a tangential direction to enhance the rotation of the steam-water mixture. The water droplets are thrown to the wall of the skimmer cylinder, forming a water film which flows into the separation box through skimmer slots, and finally return to the SG recirculating water by the drain tube. Most of the steam flows out from the outlet of the secondary separator, and a small amount of steam entering the separation box flows out from the bypass holes.
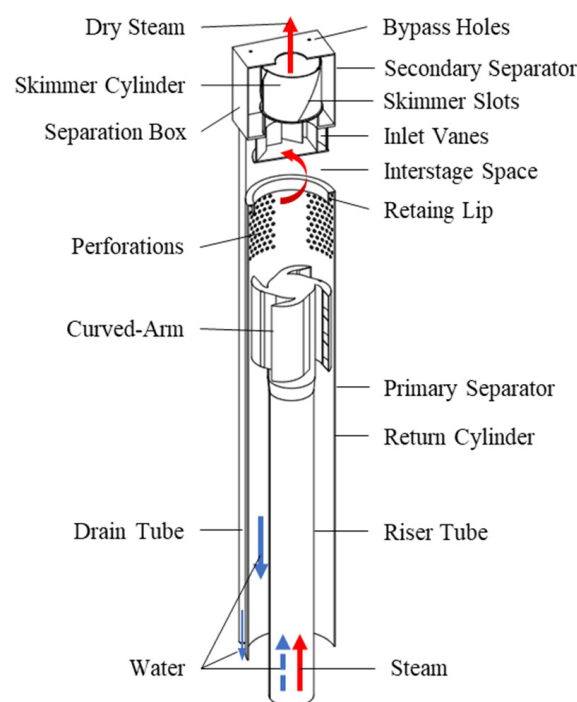
Figure 1. Structure of separation equipment.

Overload caused by uneven load distribution may occur during the operation of the separation equipment, resulting in re-entrainment and sudden rise of outlet wetness. Therefore, load margin and layout need to be considered in the design of the separation equipment. Attention should also be paid to the impact and impact corrosion of the steam-water mixture, especially at the top plate of the curved-arm, which is the first impact location, because the water has not been separated, and the density and kinetic energy of the steam-water mixture are the largest. To prevent weld failure and corrosion perforation, attention should be paid to the material selection and welding reliability. Water quality is also important, especially the dissolved salt concentration, which may cause fouling and corrosion, thus affecting the separation performance and safety of the separation equipment. Therefore, the water quality should be considered when selecting the type of the separation equipment, and should be strictly controlled during operation.

The performance of separation equipment or a separator is mainly described by the separation efficiency η, outlet wetness ω and pressure loss ΔP [1]:

$$\eta = \frac{\dot{m}_{ws}}{\dot{m}_w} \times 100\% \tag{1}$$

$$\omega = \frac{\dot{m}_{wo}}{\dot{m}_s + \dot{m}_{wo}} \times 100\% \tag{2}$$

$$\Delta P = P_{in} - P_{out} \tag{3}$$

$$P = p + \frac{1}{2}\rho_m V_m^2 \tag{4}$$

where $\dot{m}_s$ is steam mass flow at the inlet of the separation equipment, kg/s, which is also the steam mass flow of each separator due to the conservation of steam mass; $\dot{m}_w$ is the saturated water mass flow at the inlet of the separation equipment, kg/s; $\dot{m}_{wo}$ is the water mass flow at the outlet of the separation equipment, kg/s; $\dot{m}_{ws}$ is the amount of water separated, kg/s, and $\dot{m}_{ws} = \dot{m}_w - \dot{m}_{wo}$; P_{in} is the inlet total pressure, Pa; P_{out} is the outlet total pressure, Pa; ρ_m is the density of the steam-water mixture, kg/m^3; V_m is the velocity of the steam-water mixture, m/s. In the following, p and s are added after the existing subscript letters to represent the primary separator and the secondary separator, respectively.

Outlet wetness ω_p of the primary separator can be calculated by its separation efficiency η_p and circulation ratio CR.

$$\omega_p = \frac{(1 - \eta_p)(CR - 1)}{1 + (1 - \eta_p)(CR - 1)} \times 100\% \tag{5}$$

where $CR = \frac{\dot{m}_s + \dot{m}_w}{\dot{m}_s}$. While outlet wetness ω_s of the secondary separator, that is, outlet wetness of the equipment, can be calculated by its separation efficiency η_s and inlet wetness, equaling to ω_p as the gravity separation effect at the interstage space is ignored because the space is significantly small.

$$\omega_s = \frac{(1 - \eta_s)\omega_p}{1 - \eta_s\omega_p} \times 100\% \tag{6}$$

It means that ω_p depends on η_p for a given CR, while ω_s depends on both η_p and η_s.

3. Calculation Model

3.1. Geometry and Mesh

To consider the influence of other separators, the outer space is added in the calculation domain. Its shape and size are determined according to the number and distribution of the separation equipments in the SG [28–30]. The cross section of the outer space is square

(Figure 2), which is the same as the shape of the separation box. The side length of the square is 412 mm, according to the center distance of the separation equipments. To improve the calculation convergence, the calculation domain is extended by 2.5 times the side length. The bottom of the curved-arm is set to $Z = 0$, and the inlet of the riser tube of the primary separator is set to $Z = -1000$ mm, which is also the position of the normal water level.
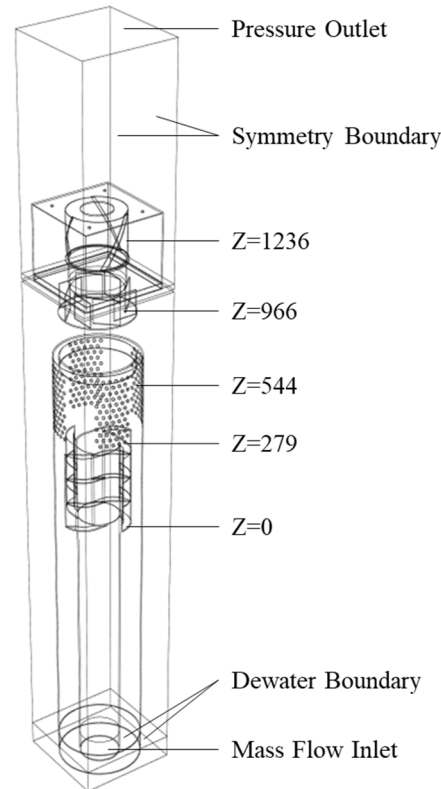
Figure 2. Calculation zone and boundary conditions.

The calculation domain is divided with hybrid grids. Structured meshes are used for regular areas such as the riser tube and outer space. For irregular zones such as holes, thin plates, and gaps, unstructured meshes are used; the mesh is densified at places where the velocity and phase volume fraction change rapidly, such as the curved-arm, the perforations and the skimmer slots. The number of grids was increased from 8 million to 15 million to meet the mesh independence, and finally, 11 million hybrid grids were used, taking into account the computing accuracy and resources.

3.2. Mathematical Model

Control equation: the steam and water in the separation equipment are regarded as continuous fluid and quasi-fluid, respectively, and the continuous Equation (6) and momentum Equation (7) are solved. It is considered no mass or heat transfer between the two phases. The turbulence model selects the Realizable *k-ε* model [12,26] with good convergence and reliability. The standard wall function is chosen to solve the near-wall region. The Eulerian multiphase flow model is adopted for the two-phase flow simulation.

$$\frac{\partial(\alpha_i \rho_i)}{\partial t} + \nabla \cdot \left(\alpha_i \rho_i \vec{u}_i\right) = 0 \tag{7}$$

where α_i is volume fraction of phase i; ρ_i is density of phase i; $\vec{u}_i$ is velocity of phase i, m/s; $i = g, l$, respectively, for gas and liquid, and $\alpha_l + \alpha_g = 1$.

$$\frac{\partial\left(\alpha_i\rho_i\vec{u}_i\right)}{\partial t} + \nabla \cdot \left(\alpha_i\rho_i\vec{u}_i\vec{u}_i\right) = -\alpha_i\nabla p + \nabla \cdot \tau_i + \alpha_i\rho_i g + F_i \tag{8}$$

where, p is pressure, Pa; g is gravitational acceleration, 9.81 m/s^2; τ_i is tangential stress of the phase i; F_i is inter-phase force, including drag force, lift force and virtual mass force. The expression of drag force is:

$$F_{l,D} = \frac{3}{4}\alpha_g\rho_l\frac{C_D}{x}\left|\vec{u}_g - \vec{u}_l\right|\left(\vec{u}_g - \vec{u}_l\right) \tag{9}$$

where x is water droplet diameter, mm; C_D is drag coefficient.

The Schiller and Naumann models commonly used in the literatures [26] is:

$$C_D = \begin{cases} 24/Re\left(1 + 0.15Re^{0.687}\right) & Re \leq 1000 \\ 0.44 & Re > 1000 \end{cases} \tag{10}$$

Boundary conditions: the inlet of the primary separator is also the inlet of the separation equipment, where a mixture of saturated steam and water enters. The mass inlet boundary is adopted, and the mass flow of steam and water are given, respectively. The top outlet boundary is set as the pressure outlet, and the bottom outlets of the return cylinder and the outer space are set as the dehydration boundary using the user-defined function (UDF) [26], that is, water droplets can pass through but steam cannot, to simulate the impact of water level; the four sides of the outer space use symmetric boundary to reflect the influence of other separation equipment around. The effect of gravity is considered.

Solution format: Phase Couple SIMPLE algorithm is used to solve the pressure-velocity coupling, and the second-order upwind scheme is used for spatial discretization. ANSYS FLUENT 15.0 is used as the computing platform. Unsteady calculation method is adopted, and the time step is 0.0001 s.

Calculation condition: the pressure of the saturated steam is 4.7 MPa (260 °C), and steam load is 100% ($\dot{m}_s$ = 3.91 kg/s), CR = 6 ($\dot{m}_w$ = 19.55 kg/s). To carry out the numerical calculation, it is necessary to give a specific droplet diameter value. The droplet diameter range set in literature [26] is 0.1~150 μm. Since we mainly focus on the droplet diameter that has a significant impact on the performance of the separator, we decided to start from 50 μm. The last droplet diameter value far exceeds the upper limit of that in literature [26], and reaches 400 μm. Five different droplet diameters were chosen finally, i.e., 50 μm, 100 μm, 200 μm, 300 μm, and 400 μm. Each case takes 20–24 days on the workstation with two CPUs (Intel (R) Xeon (R) Platinum 8375C, main frequency 3.50 GHz, 64 cores).

4. Analysis and Discussion

4.1. Performance Analysis of Separation Equipment

Figures 3–5 show the separation efficiency η, outlet wetness ω, and pressure loss ΔP of the separation equipment and each separator, variating with the droplet diameter x. With the increase in droplet diameter, the separation efficiency of the separation equipment and each separator gradually increases, and the outlet wetness gradually decreases. When $x \geq 200$ μm, the separation efficiency of the separation equipment and the primary separator changes from rapid to slow growth, while the separation efficiency of the secondary separator turns to slow growth as $x \geq 300$ μm. The separation efficiency of the primary separator increases, making the water mass flow entering the secondary separator decrease with the droplet diameter, causing the separation efficiency of the secondary separator to be affected by the inlet wetness and droplet diameter at the same time and the variation trend differing from that of the primary separator. Since the majority of the water is separated by the primary separator, the separation efficiency trend of the entire separation equipment

is similar to that of the primary separator. Literature [20,21] points out the separation efficiency of the primary separator $\eta_p \geq 95\%$, and outlet wetness $\omega_p \leq 20\%$, corresponding to $x \geq 300$ μm, and the outlet wetness of the separation equipment during actual operation $\omega \leq 0.1\%$ [1], corresponding to $x \geq 400$ μm.
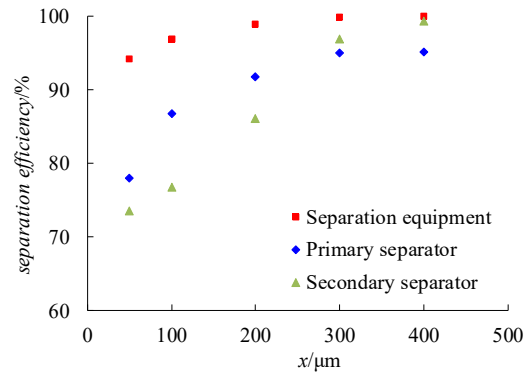
Figure 3. Separation efficiency of separation equipment and each separator.
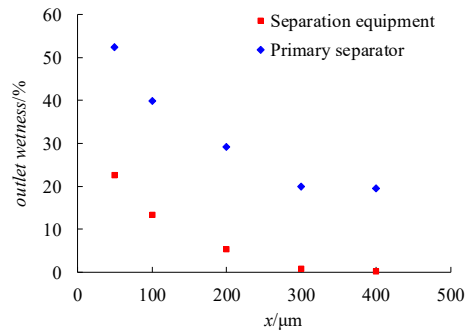
Figure 4. Outlet wetness of separation equipment and primary separator.
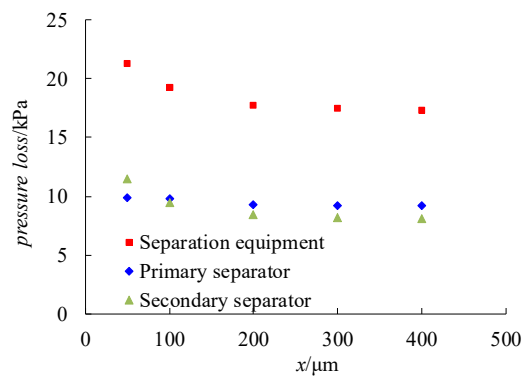
Figure 5. Pressure loss of separation equipment and each separator.

With the increase in droplet diameter, the pressure loss of the separation equipment and each separator first decreased and then stabilized. Within the selected droplet diameter range, the maximum difference of pressure loss ΔP_p of the primary separator is only 0.64 kPa, and the ratio of the maximum to the minimum pressure loss is 1.07; therefore, the pressure loss of the primary separator is slightly affected by the droplet diameter. The maximum difference of pressure loss ΔP_s of the secondary separator reaches 3.31 kPa, and the ratio of the maximum to the minimum pressure loss is 1.41. When $x \geq 100$ μm, the pressure loss of the primary separator exceeds that of the secondary separator, because the inlet wetness of the secondary separator decreases with the increase in droplet diameter, and energy consumed by separating water droplets is reduced, resulting in decrease in

pressure loss. The variation pressure loss of the secondary separator is apparent, hence, the pressure loss variation trend of the entire separation equipment is similar to it. Generally, the pressure loss of the swirl-vane separator is much higher than that of the corrugated-plate separator [1], while the pressure loss of the curved-arm separator is close to that of the axial flow separator. The pressure loss of the curved-arm separator is 9.2~9.8 kPa, about half of that of the swirl-vane separator (18.9 kPa at normal working condition [26]), and is conducive to achieving a higher circulation ratio.

The pressure loss of the separation equipment is not given in literature [20,21], and the calculation accuracy of the pressure loss cannot be directly verified. However, the relative deviation between the calculated pressure loss of the swirl-vane separator and the test value is within 4.8% [26]. The same calculation method is adopted, and the pressure loss calculated in this paper has a certain degree of reliability consequently. Therefore, the prediction of separation efficiency and pressure loss is more accurate with $x = 400$ μm as the characteristic value of the actual inlet droplet diameter distribution.

4.2. Internal Flow Analysis of Separation Equipment

Figures 6–8 show the distribution of different flow characteristic parameters in the separation equipment under different droplet diameters. Sections of $Z = 279$ mm and $Z = 544$ mm correspond to the center position of the upper channel of the curved-arm and the perforation of the return cylinder, respectively, and sections of $Z = 966$ mm and $Z = 1236$ mm correspond to the center position of the inlet vanes and the skimmer cylinder, respectively. Flow characteristic parameters at the inlet of the primary separator can be calculated according to the flow and physical properties, i.e., the water volume fraction $\beta = 0.132$, steam velocity $u_s = 9.2$ m/s, and turbulent kinetic energy $K_s = 0.32$ m^2/s^2.

4.2.1. Phase Volume Fraction Distribution

Section $Y = 0$ of the separation equipment in Figure 6 shows that with the increase in droplet diameter, the water film ($\beta = 1.0$) gradually thickens, especially at the inner side of the top plate of the curved-arm, the perforations, and the upper part of the skimmer cylinder. The larger the droplet diameter, the greater the centrifugal force, and the easier it is to reach the wall and form a water film.

The water film at the inner side of the top plate of the curved-arm is formed due to the inertia of water droplets, which deposit after colliding with the top plate. The thickness of the water film at the lower end of the return cylinder gradually increases with the droplet diameter, indicating that more water flows downward to the recirculating water. After the water film in the curved-arm flows out, it melts into the water film on the inner wall of the return cylinder. These water films also thicken with the increase in droplet diameter (see section $Z = 279$ mm). When $x = 400$ μm, the water film at the perforations no longer presents a regular ring, and is stripping off due to re-entrainment. The thicker the water film is, the easier the interface instability of the steam-film is to spread, and the water film is torn (see section $Z = 544$ mm). The water film at the perforations is sprayed through the drain holes to the outer space (see section $Z = 544$ mm). Water flows out of the drain holes diagonally and does not fill the drain holes. The water film moves in a circumferential direction, and the drain holes are perpendicular to the cylinder wall, that is, perpendicular to the movement direction of the water film, which is not conducive to water drainage, causing the water film to become thicker. Therefore, the distribution and angle of the drain holes should be optimized.

When $x \leq 100$ μm, the water flow from the perforations diffuses in the outer space (see section $Z = 544$ mm) and is carried upward by the steam, resulting in high outlet wetness. When $x \leq 200$ μm, this phenomenon is gradually less obvious. When the droplet diameter further increases, re-entrainment occurs at the perforations, slowing down the growth of the separation efficiency of the primary separator.
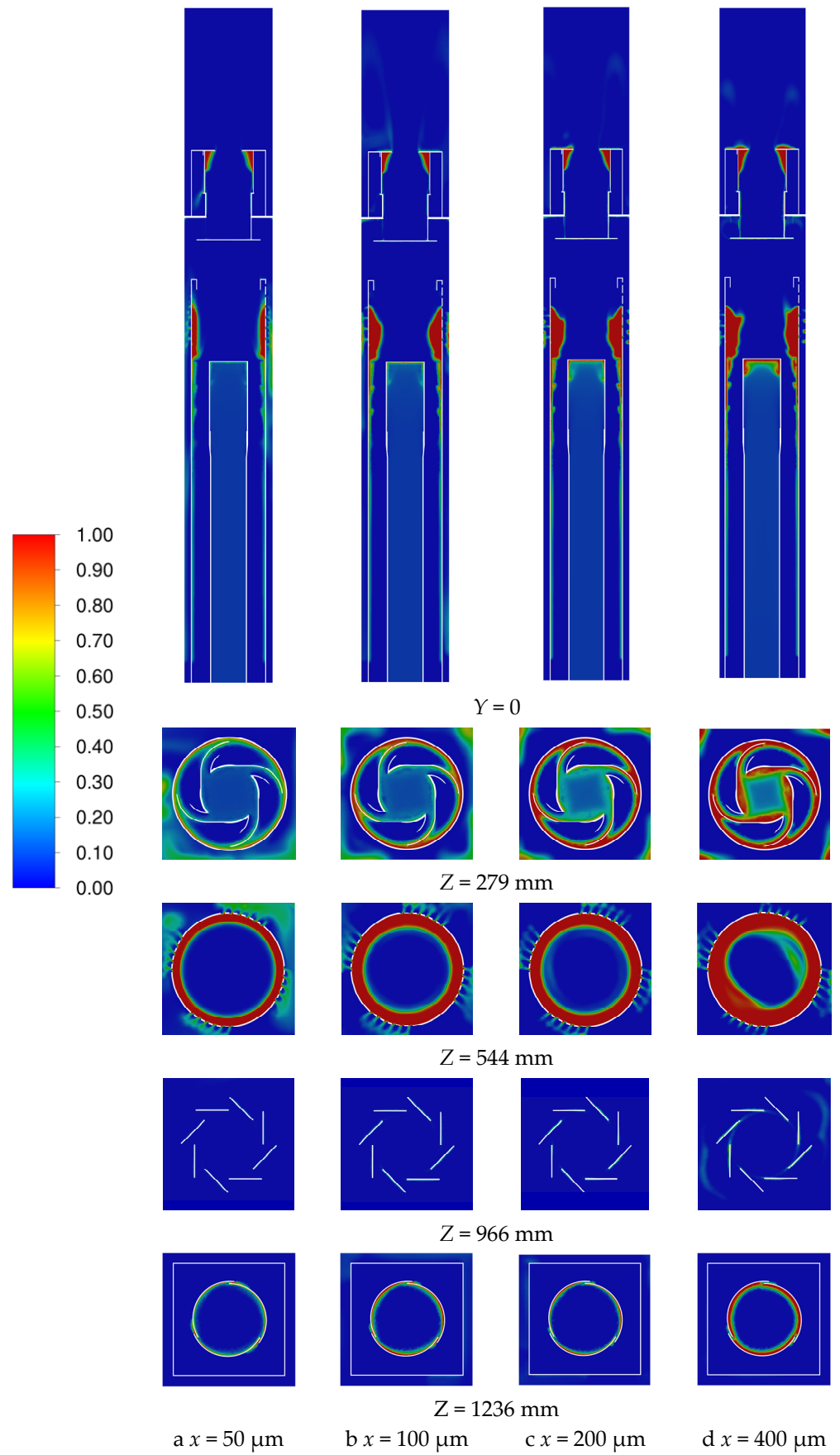
Figure 6. Distribution of water volume fraction.
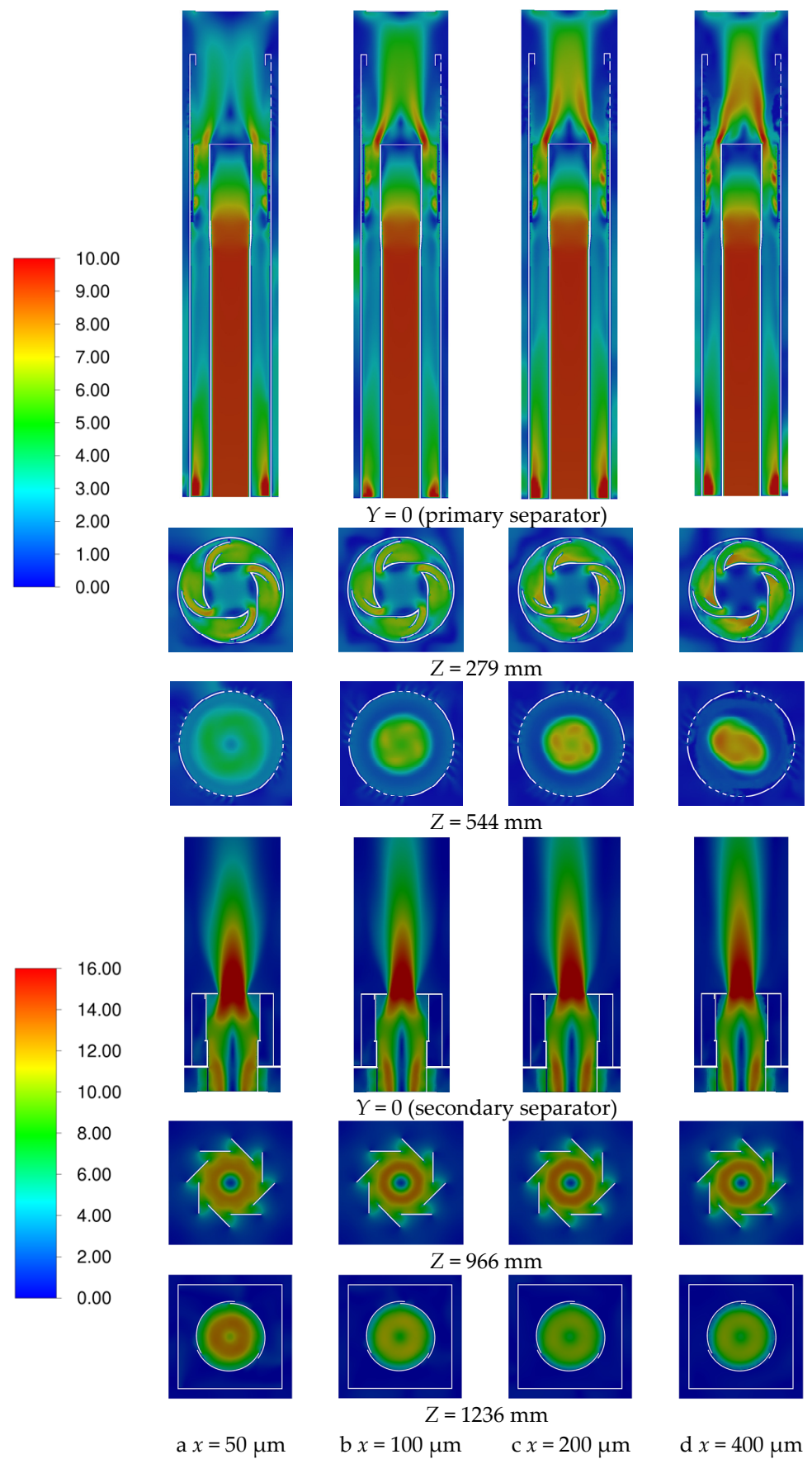
Figure 7. Distribution of Steam Velocity (unit: m/s).
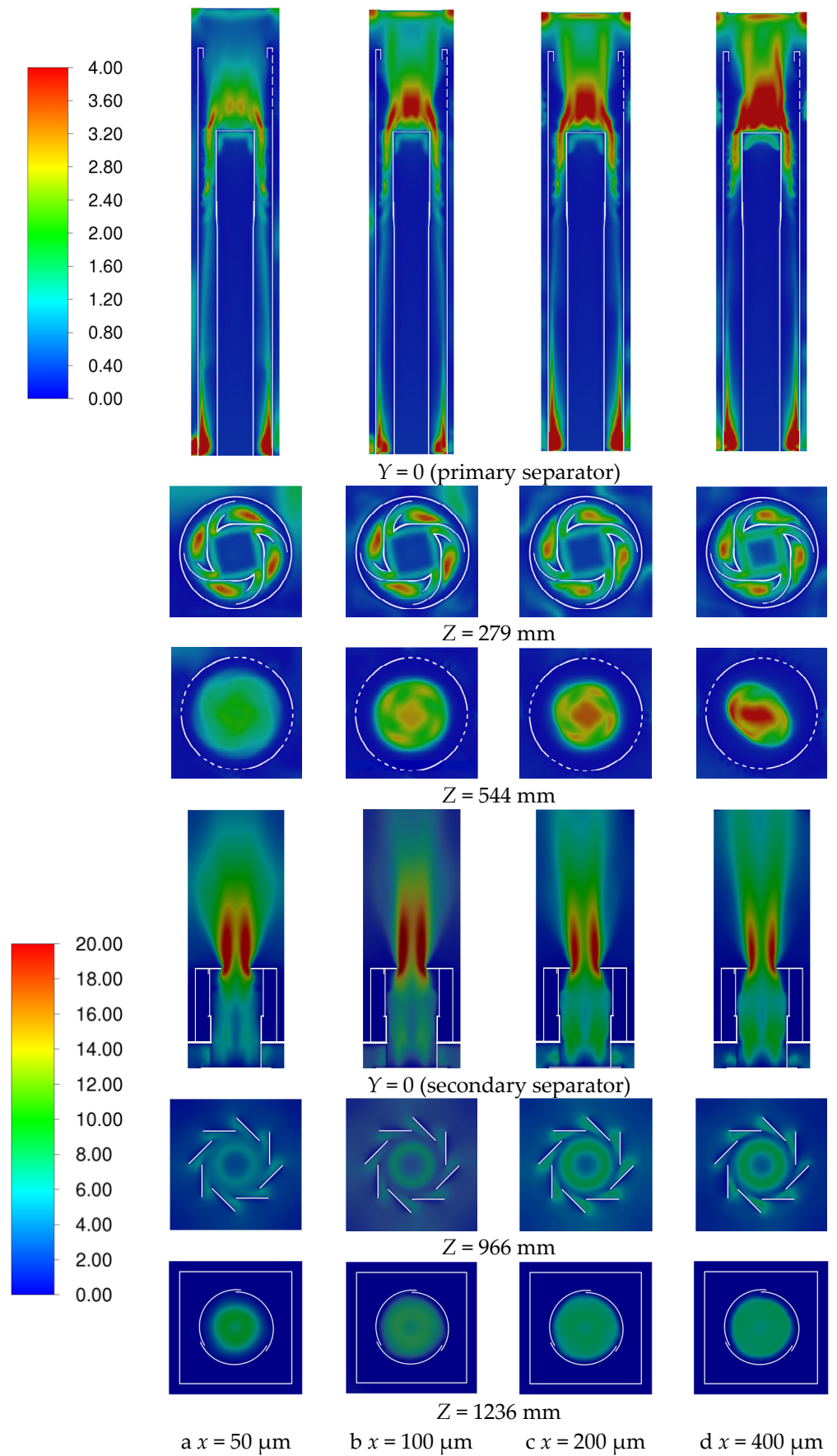
Figure 8. Turbulent kinetic energy distribution of steam-water mixture (unit: m^2/s^2).

As the water droplet diameter increases, the ability of steam to carry water droplets decreases and part of the water droplets deposit on the inlet vanes of the secondary separator (see section $Z = 966$ mm). When $x = 400$ μm, due to the thickening of the water film, the water droplet wake appears at the end of the inlet vanes.

The thickness of the water film inside the skimmer cylinder also increases significantly, and flows into the separation box from the skimmer slots (see section $Z = 1236$ mm). The water film moves upward under the shear stress of steam, and is blocked by the top plate due to untimely drainage, which makes the water film gradually thicken along the height direction. When $x \geq 100$ μm, the water droplet wake produced by the re-entrainment can be seen at the outlet of the secondary separator, and a small amount of water film overflows and accumulates above the top plate (see section $Y = 0$). Therefore, the skimmer slots should be optimized to further improve the drainage capacity.

4.2.2. Velocity Distribution

Since the flow velocity and turbulent kinetic energy values inside the secondary separator are significantly higher than that inside the primary separator, different legends are used for easy display, respectively.

Section $Y = 0$ in Figure 7 shows the steam velocity decreases after entering the curved-arm, and the low-velocity region near the top plate gradually expands with the increase in water droplet diameter, caused by steam outflow from branches. Due to the gradual thickening of the water film on the wall of the return cylinder reducing the flow area, the steam gradually shrinks to the center, squeezing the wake region and increasing its velocity (see section $Z = 544$ mm). The flow core above the curved-arm is swirling and impacts the bottom of the secondary separator, and then enters the inlet vanes.

Section $Z = 279$ mm shows with the increase in droplet diameter, the steam velocity in the upper channel of the curved-arm gradually decreases, because the droplets deposited in the upper channel increases the flow resistance of the steam, making the steam flow out through the other lower channels. Since the water film on the return cylinder gradually thickens, the flow area of the rising steam between the curved-arm and the return cylinder reduces, and the steam velocity increases. Although the high-velocity regions increase with the droplet diameter, the pressure loss decreases instead, because the density of mixture decreases significantly due to the improvement of separation efficiency. The steam velocity at the curved-arm outlet is 6~8 m/s, and less than the steam velocity in the riser tube. However, the curved-arm outlet is close to the inner wall of the return cylinder; therefore, the water film and water droplets can reach the wall surface more quickly.

The inlet vanes of the secondary separator strengthen the rotation of the steam flow. The velocity value at the inlet vane outlet reaches 12~13 m/s (see section $Z = 966$ mm), which is nearly twice that at the outlet of the curved-arm. Because of the small radius of rotation, the steam can generate greater centrifugal force, which is conducive to the separation of smaller water droplets. A low-velocity region forms at the center of the rotating steam flow and disappears before reaching the middle of the skimmer cylinder (see section $Y = 0$ and $Z = 1236$ mm), due to squeezing by the steam flow. The rotation gradually weakens in the upward movement, and the velocity reaches its maximum at the outlet due to the sudden reduction in flow area, resulting in high throttling loss. The steam jet is formed at the secondary separator outlet, and its jet core increases with the droplet diameter (see section $Y = 0$).

4.2.3. Turbulent Kinetic Energy Distribution

Section $Y = 0$ in Figure 8 shows that the high K_s region in the primary separator is mainly distributed in the flow channels of the curved-arm, the steam rising channel between the curved-arm and the return cylinder, and above the curved-arm, that is, the pressure loss is mainly generated in these three regions. With the increase in water droplet diameter, the high K_s region and value above the curved-arm increase (see section $Y = 0$ and $Z = 544$ mm), including the region under the bottom plate of the secondary separator. However, the

increase in high K_s region and value does not make ΔP_p increase, but decrease, because the separation efficiency increases with the droplet diameter, and the density of the mixture decreases significantly. Due to the small value of K_s, within 8 m^2/s^2, ΔP_p varies slowly. The rotating steam flow impacting the bottom plate of the secondary separator also produces large pressure loss, which cannot be accurately calculated by separated simulation of the two separators.

The inlet vane region, the skimmer cylinder region, and the jet core above the secondary separator are all high K_s regions (section $Y = 0$) and up to 26 m^2/s^2, which is more than three times that of the primary separator, hence, the pressure loss of the secondary separator is relatively large. With the increase in droplet diameter, the high K_s region inside the secondary separator increases, while the high K_s region in the jet core above the outlet decreases. ΔP_s showed a trend of decreasing rapidly and then slowly, because the water mass entering the secondary separator decreases with the same variation trend.

5. Conclusions

(1) The integrated calculation and analysis of the separation equipment can more truly reflect the flow state between the primary and secondary separators, especially the inlet parameters of the secondary separator, improving the reliability of the performance prediction and mechanism analysis.

(2) With the increase in water droplet diameter, the separation efficiency of the separation equipment and each separator gradually increases, the outlet wetness gradually decreases, and the pressure loss first decreases and then stabilizes. When 400 μm is selected as the characteristic value of the actual inlet droplet diameter distribution, the performance prediction of the separation equipment is more accurate.

(3) The pressure loss of the primary separator is less affected by the droplet diameter, while the inlet wetness of the secondary separator decreases with the increase in the droplet diameter, and its pressure loss variation is more obvious, so the pressure loss variation trend of the separation equipment depends on the secondary separator. The majority of the water is separated by the primary separator, so the variation trend of the separation efficiency of the separation equipment depends on the primary separator.

(4) Different from the traditional separation equipment, the pressure loss of the two separators of this separation equipment is relatively close. The pressure loss of the primary separator is significantly less than that of the swirl-vane primary separator, which is conducive to achieving a higher circulation ratio.

(5) With the increase in droplet diameter, the water film inside the separation equipment thickens, re-entrainment appears at the perforations of the primary separator and the outlet of the secondary separator, which makes the growth of the separation efficiency of the separation equipment and each separator slow down. Therefore, the structure of the perforations and skimmer slots should be optimized to further improve the drainage capacity and separation efficiency.

Author Contributions: Conceptualization, X.Y.; methodology, C.Z.; validation, Q.Z. and J.C.; formal analysis, X.Y.; writing—original draft preparation, C.Z.; writing—review and editing, X.Y.; supervision, J.M. All authors have read and agreed to the published version of the manuscript.

Institutional Review Board Statement: Not applicable.

Informed Consent Statement: Not applicable.

Data Availability Statement: Not applicable.

Conflicts of Interest: The authors declare no conflict of interest.

Nomenclature

CFD	computational fluid dynamics
C_D	drag coefficient
CR	circulation ratio
ΔP	pressure loss
F_i	inter-phase force
g	gravitational acceleration(9.81 m/s^2)
K_s	turbulent kinetic energy
$\dot{m}_s$	inlet saturated steam mass flow (kg/s)
$\dot{m}_w$	inlet saturated water mass flow (kg/s)
$\dot{m}_{wo}$	outlet water mass flow (kg/s)
$\dot{m}_{ws}$	separated water mass flow (kg/s)
P_{in}	inlet total pressure (Pa)
P_{out}	outlet total pressure (Pa)
PWR	pressurized water reactor
SG	steam generator
u_s	steam velocity
V_m	velocity of steam-water mixture (m/s)
x	water droplet diameter (mm)
β	water volume fraction
ω	outlet wetness
η	separation efficiency
ρ_m	density of steam-water mixture (kg/m^3)

References

1. Green, S.J.; Hetsroni, G. PWR steam generators. *Int. J. Multiph. Flow* **1995**, *21*, 1–97. [CrossRef]
2. Zhang, Q.; Chen, W. Experimental study on performance optimization for full-scale swirl separator of air-water in PWR UTSG. *Progr. Nucl. Energy* **2021**, *142*, 104011. [CrossRef]
3. Mauro, G.; Sala, M.; Hetsroni, G. Improved Italian moisture separators (IIMS). *Nucl. Eng. Des.* **1990**, *118*, 179–192. [CrossRef]
4. Kim, W.S.; Lee, J.B.; Kim, K.H. Development of empirical correlation of two-phase pressure drop in moisture separator based on separated flow model. *Energies* **2021**, *14*, 4448. [CrossRef]
5. Xiong, Z.; Lu, M.; Wang, M.; Gu, H.; Cheng, X. Study on flow pattern and separation performance of air–water swirl-vane separator. *Ann. Nucl. Energy* **2014**, *63*, 138–145. [CrossRef]
6. Baltrėnas, P.; Chlebnikovas, A. Removal of fine solid particles in aggressive gas flows in a newly designed multi-channel cyclone. *Powder Technol.* **2019**, *356*, 480–492. [CrossRef]
7. Zhou, W.; Chenglin, E.; Fan, Y.; Wang, K.; Lu, C. Experimental research on the separation characteristics of a gas-liquid cyclone separator in WGS. *Powder Technol.* **2020**, *372*, 438–447. [CrossRef]
8. Yao, X.; Zuo, P.; Lu, C.; Chenglin, E.; Liu, M. Characteristics of flow and liquid distribution in a gas–liquid vortex separator with multi spiral arms. *Particuology* **2022**, *68*, 101–113. [CrossRef]
9. Wang, M.; Wang, Y.; Tian, W.; Qiu, S.; Su, G. Recent progress of CFD applications in PWR thermal hydraulics study and future directions. *Ann. Nucl. Energy* **2021**, *150*, 107836. [CrossRef]
10. Liu, K.; Wang, M.; Gan, F.; Tian, W.; Qiu, S.; Su, G. Numerical investigation of flow and heat transfer characteristics in plate-type fuel channels of IAEA MTR based on OpenFOAM. *Prog. Nucl. Energy* **2021**, *141*, 103963. [CrossRef]
11. Zhao, X.; Wang, M.; Chen, C.; Wang, X.; Ju, H.; Tian, W.; Qiu, S.; Su, G. Three-dimensional study on the hydraulic characteristics under the steam generator (SG) tube plugging operations for AP1000. *Prog. Nucl. Energy* **2019**, *112*, 63–74. [CrossRef]
12. Zhao, F.; Zhao, C.; Bo, H. Numerical investigation of the separation performance of full-scale AP1000 steam-water separator. *Ann. Nucl. Energy* **2018**, *111*, 204–223. [CrossRef]
13. Zhang, H.; Liu, Q. Numerical investigation on performance of moisture separator by Lagrangian-Eulerian strategy: Physical mechanisms, theoretical models, and advanced algorithms. *Ann. Nucl. Energy* **2020**, *137*, 107081. [CrossRef]
14. Du, L.; Zhang, H.; Tian, R.; Zhang, P. Analysis of factors affecting the separation efficiency in corrugated plate steam separator. *At. Energy Sci. Technol.* **2018**, *52*, 802–807. (In Chinese)
15. Zhu, Y.; Wang, X.; You, E.; Huang, D.; Zhao, F. Optimization of drain hook of double hook corrugated plate steam water separator. *At. Energy Sci. Technol.* **2021**, *55*, 1780–1787. (In Chinese)
16. Cai, Z.; Wang, P.; Luo, X.; Huang, J.; Qin, Z.; Mei, J.; Zhao, W. Numerical Investigation on the Influence of Class Number and Wavelength on the Performance of Curved Vane Demisters. *Atmosphere* **2022**, *13*, 1711. [CrossRef]
17. Li, S.; Wang, P.; Luo, X.; Wang, Y.; Yang, X.; Thakur, A.K.; Zhao, W. Numerical analysis of chevron demisters with drainage hooks in optimizing separation performance. *Int. J. Heat Mass Transf.* **2020**, *152*, 119522. [CrossRef]
18. Wang, P.; Jiang, J.; Li, S.; Yang, X.; Luo, X.; Wang, Y.; Thakur, A.K.; Zhao, W. Numerical investigation on the fluid droplet separation performance of corrugated plate gas-liquid separators. *Sep. Purif. Technol.* **2020**, *248*, 117027. [CrossRef]

19. Ding, X. Water circulation and Analysis on the secondary side of steam generator. *Nucl. Power Plant* **2002**, *8*, 1–8. (In Chinese)
20. Reed, M.J.; Prueter, W.P.; Caple, P.; Boyd, T. High-efficiency separation equipment for use in recirculating steam generators. In Proceedings of the ASME Winter Conference, New Orleans, LA, USA, 28 November–3 December 1993; pp. 1–7.
21. Prueter, W.P.; Birmingham, D.P.; Reed, M.J. Compact, High-Efficiency, Gas/Liquid Separator Method and Apparatus. U.S. Patent 6,364,940, 2 April 2002.
22. Dyke, J.M.; Garland, W.J. Evolution of CANDU Steam Generators—A Historical View. *Canteach Publ.* **2006**, 1–15.
23. Ding, X. Summarization of CANDU Steam Generator Design. *Nucl. Power Eng.* **1998**, *19*, 56–63. (In Chinese)
24. Liu, Y.; Ke, B.; Wang, X.; Yang, X.; Tian, R. Study on separation performance of two-stage cyclone steam water separator. *Nucl. Power Eng.* **2020**, *41*, 114–119. (In Chinese)
25. Liu, Y.; Yang, X.; Ke, B.; Wang, X.; Tian, R. Numerical study on structural optimization of two-stage cyclone steam water separator. *J. Harbin Eng. Univ.* **2018**, *39*, 1308–1313. (In Chinese)
26. Yang, X.L.; Wang, Y.; Feng, J.; Wang, W.; Wang, X.Y. Effect of droplet size on swirl vane separator performance. *At. Energy Sci. Technol.* **2016**, *50*, 2200–2205. (In Chinese)
27. Katono, K.; Ishida, N.; Sumikawa, T.; Yasuda, K. Air–water downscaled experiments and three-dimensional two-phase flow simulations of improved steam separator for boiling water reactor. *Nucl. Eng. Des.* **2014**, *278*, 465–471. [CrossRef]
28. Dahlin, E. Advancing CANDU experience to the world steam generator market. In Proceedings of the CNA/CNS Conference, Fredericton, NB, Canada, 9–12 June 1996. INIS-CA-0056.
29. Naraine, M.; Riznic, J. The current status of CANDU steam generators. In Proceedings of the International Conference on Nuclear Engineering, Shanghai, China, 2–6 July 2017; American Society of Mechanical Engineers: New York, NY, USA, 2017; Volume 57878, p. V009T15A001.
30. Riznic, J. *Steam Generators for Nuclear Power Plants*; Woodhead Publishing: Cambridge, UK, 2017; p. 67.